Civil and Environmental Engineering
Vol. 0, Issue 0, DOI: 10.2478/cee-2026-0069

Flow Velocity Distribution near Curb-opening Inlets: Experiments and Analysis

Zaid H. HASAN[1,*], Mohammed A. Almajeed A ALABAS[1]

[1] Department of Civil Engineering, College of Engineering, University of Babylon, Babylon, Iraq.

* corresponding author: Zaid.Hussein.engh335@student.uobabylon.edu.iq

Date of Submission: 07 November 2025
Revision Date: 23 November 2025
Date of Acceptance: 24 November 2025

Civil and Environmental Engineering
Journal of the Faculty of Civil Engineering | University of Žilina

Abstract

This paper presents an experimental investigation of the velocity distribution around curb-opening inlets using a laboratory channel model measuring 6.2 m in length, 2 m in width, and 1. 5 m in height. The flow system consisted of a base discharge supplemented by a spatially varied inflow generated through twelve nozzles uniformly arranged along the model's length and width. Velocity measurements were carried out with a laser Doppler velocimeter (LDV) to examine the applicability of the universal velocity profile in accordance with the law of the wall. Dimensional analysis was employed to identify the governing parameters and construct a representative diagram for flow characterization. Under uniform flow conditions, without nozzle-induced inflow, the velocity distribution exhibited close agreement with the universal velocity profile. In contrast, the introduction of spatially varied inflow resulted in significant deviations, particularly within the buffer layer and logarithmic region, with discrepancies becoming more pronounced downstream as the cumulative influence of multiple nozzles increased. The measurements further revealed that the nozzle inflow generates a localized jet within the viscous sublayer, and the intensity of this jet was observed to increase in the downstream direction in response to higher inflow discharge. These findings highlight the complex interaction between localized inflow and classical velocity distribution laws.

Keywords

Spatially varied flow; Velocity distribution; Curb opening inlet; Log law; Viscous sublayer.

1. Introduction

The number of heavy rainfall events increased due to climate change, so controlling urban floods is becoming increasingly crucial (Kemper, S., & Schlenkhoff, A. 2019; Gómez, M., & Russo, B. 2009). This increase must be matched by the development of sewerage systems and accessories to accommodate these additional quantities, because the ineffective drainage system causes many road problems, including floods, traffic accidents, and road damage, in addition to being considered an uncivilized phenomenon (Pedro et al., 2016; Alfatlawi et al., 2021). To lower these dangers, and surface drainage systems need to be precisely and meticulously designed to prevent damage during severe storm events in urban areas (Russo, 2010; Garcia et al., 2019). Curb opening inlets are usually found in places with pavement, such as parks, squares, airport aprons, and pedestrian zones, and are installed in street gutters and sump locations (Tiğrek, Ş., &

Sipahi, S., 2012). In these areas, isolated inlets are unable to collect all the storm-related runoff into the sewage system, since there are not a clear flow channels or sufficient gradients to guide the flow toward the collecting hydraulic structures (Russo et al., 2013).

It is important to study all the parameters that accompany this phenomenon and contribute to solving these problems and designing an efficient sewage system to drain water from the roads. Among these important parameters in this regard is how velocity is distributed on the road and around the curb opening inlets and what are the important parameters that influence on velocity distribution (Comport & Thornton, 2012).

Therefore, this paper addresses this topic due to its importance, focusing on the distribution of velocity in a model subjected to spatially varied (SV) flow introduced through twelve uniformly arranged nozzles located above the physical model. In such flows, the discharge progressively increases in the downstream direction, a condition referred to as spatially varied flow with increasing discharge. Analytical investigations of this type of flow have traditionally relied on one-dimensional formulations, where the continuity equation combined with the principle of linear momentum is employed to derive governing relations for the variation of water surface elevation (Khiadani et al., 2007; Beecham et al., 2005).

The velocity distribution in uniform open-channel flows can be divided into four distinct regions: the viscous sublayer (Y^+<5-10), where the linear relationship $U^+ = Y^+$ is valid. The buffer layer ($5<Y^+<30$), in which the mixing length can be expressed as:

$l^+=kY^+ \Gamma (Y^+)$, with $\Gamma (Y^+) =1-\exp (-Y^+/B_d)$. B_d empirically determined = 26 for boundary layers, a value later confirmed for open-channel flows by Nezu & Rodi (1986) & Van Driest (1956). The log-law or inertial sublayer ($30 < Y^+ < 0.2R^*$), where the velocity profile follows $U^+ = (1/\kappa) \ln(Y^+) + C$, with $\kappa = 0.41$ and $C = 5.29$. The velocity-defect law region ($Y^+ > 0.2R^*$) applies, where the velocity distribution is described as: $U^+ = (1/\kappa) \ln(Y^+) + C + w(y/h)$ (Nezu & Rodi, 1986; Nezu, I., & Nakagawa, H., 1993).

In this paper, the nozzles were employed to reproduce a controlled, cumulative discharge increase along the flume length, consistent with laboratory procedures commonly adopted in previous SVF studies.

Several previous studies have simulated spatially increasing discharge using point or discrete inflow sources instead of a continuous lateral slot or porous boundary. Henderson (1966) argued that discrete inflows can faithfully represent the continuous discharge variations found in natural systems when the local mixing length is small relative to the spacing of the inflow points. Chow (1959) similarly noted that SVF may be modelled using either a continuous inflow boundary or an equivalent set of discrete inflows, provided these are uniformly distributed and hydraulically calibrated. Subramanya (2009) also observed that, in laboratory settings, "the continuous lateral inflow assumption can be satisfied by a number of uniformly spaced discrete inflows". Khiadani et al. (2007) employed nozzle-based inflow systems in rectangular flumes to reproduce lateral inflow in SVF with increasing discharge. Their findings indicate that when discrete inflows are sufficiently frequent and well distributed, the resulting discharge profile q(x) closely approximates that of a continuous lateral inflow, with negligible error.

Although several studies have examined spatially varied flow with increasing discharge, most investigations have focused on open-channel configurations or continuous lateral inflow boundaries. What remains largely unknown is how discrete inflow sources such as the jet like contributions from nozzles or curb-opening inlets modify the near-wall velocity structure and whether the classical log-law remains valid under such disturbances. Moreover, the interaction between localized inflow, turbulence generation, and downstream evolution of the velocity profile has not been experimentally documented for roadway drainage systems. This gap is particularly relevant because curb opening inlets receive highly non uniform inflow, yet their design typically assumes uniform or gradually varied base-flow conditions. The present paper addresses these deficiencies by providing detailed LDV measurements of velocity profiles upstream, within, and downstream of a spatially varied inflow zone representative of curb opening inlet hydraulics.

2. Experimental Procedure

An extensive experimental program of 420 tests was conducted using a rectangular model 6.2 m long, 2 m wide, and 1.5 m height, which provided sufficient length for the development of spatially varied flow under the studied conditions. Similar or shorter laboratory flumes (3–7 m) have been successfully used in previous SVF investigations (Alfatlawi, 2021; Henderson, 1966. Subramanya, K., 2009). The base discharge (Q = 10, 30, 50 m^3/hr) was regulated by a flow-meter-controlled supply system, while twelve lateral nozzles (5–12 m^3/hr each) simulated increasing discharge along the flume. In this paper, a TSI Laser Doppler Velocimeter (LDV) was employed to measure point velocities along the flow depth. The LDV is a non-intrusive optical instrument that determines instantaneous velocity components based on the Doppler frequency shift of laser light scattered by seed particles moving with the fluid (Adrian, R. J. 1991; Bonnett et al., 1995). The system uses two intersecting laser beams to form a small measurement volume (≈ 0.1 mm^3) where velocity is determined from the interference fringe spacing and the scattered light frequency. This technique provides high spatial and temporal resolution and is particularly suitable for spatially varied and turbulent flows (Tajikawa et al., 2024). Before data collection, the LDV system was calibrated according to manufacturer's procedure, and velocity measurements were taken at multiple depths at each measurement section. This ensured accurate mapping of velocity profiles and computation of depth and local flow parameters. Flow depths corresponding to each combination of Q and q were measured using an ultrasonic water-level (UWL) sensor at positions of measurement points (Figure 2); due to the similarity of the profiles, only measurements from P1–P4 were considered in the analysis. In addition, depth variations across the model width were obtained at selected locations to examine potential transverse non-uniformities in the flow.

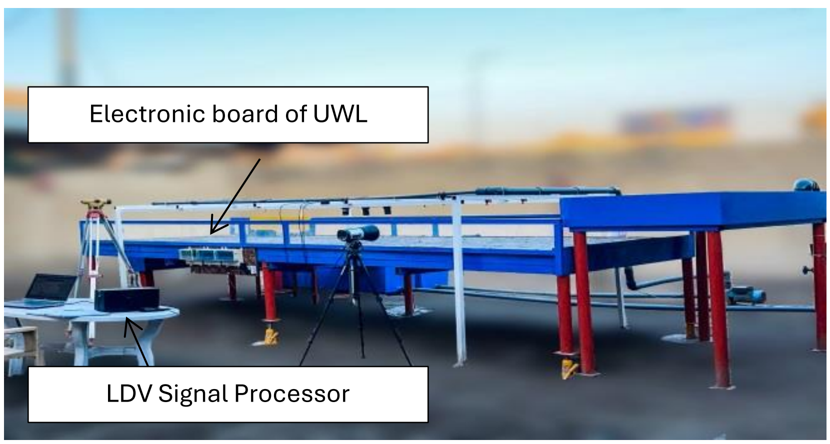

Figure 1: Experimental model equipment

Figure 2: Probe of UWL

A layer of dense asphalt was applied to the roadway section's base, which is composed of steel plate that is 3 mm thick to simulate the road surface. The side walls of the model are made of 10 mm thick Perspex to ensure clear vision (Alabas, 2025). The flow intercepted by the curb opening inlet with full-scale (which installed at 5 m from the upstream end) or the flow that bypassed it. As seen in Figure 3, for measurement, the V-notch receives the intercepted discharge. Six hydraulic jacks were positioned beneath the model's legs to adjust the model's slope.

Figure 3: Supplementary structural elements of the test model

The water supplying system consists of two 3-inch polymerized vinyl chloride (PVC) pipes of 8 m and 6.5 m in length. Two pump supplies are used to move the water from the tanks to the model, and a motorized sliding valve controls the flow that is released. The discharge is controlled by flowmeters, which used to measure the flow rate entering the model. The flow enters the tested area via a tank located upstream from the model. To guarantee that the flow entered the model uniformly, a weir was placed in the centre of the upstream tank. As seen in Figure 4, the tank dissipates flow energy and provides a horizontal pro-flow to the water's surface in the form of sheet flow.

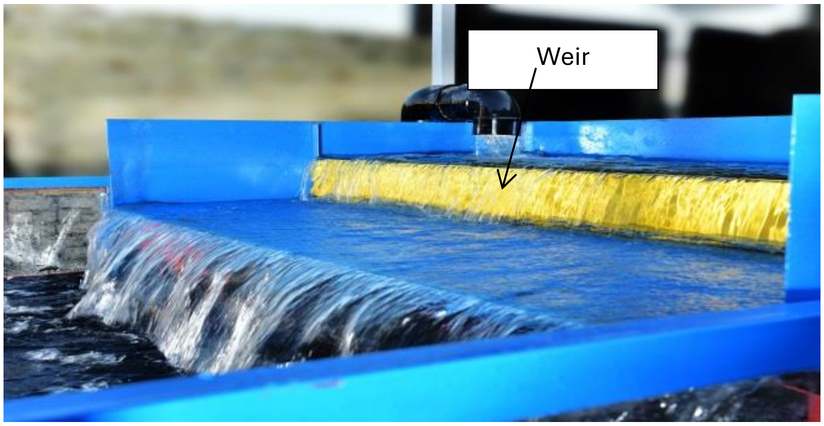

Figure 4: Sheet flow in model

The lateral inflow was provided by 12 nozzles (20 mm diameter), hoses, a supporting frame, a tank, and a pump (as shown in Figure 5). The number of nozzles (12), their spacing, and the selected discharge values were chosen to provide a gradual and evenly distributed increase in lateral inflow along the model length. This configuration follows the guidance of previous SVF studies, which demonstrated that multiple uniformly spaced discrete inflows can approximate continuous lateral inflow when the spacing is sufficiently small.

Figure 5: Nozzles in model

A steady and uniform flow may be approximated on the roadway and is either intercepted by the curb opening or bypasses and goes into the canal to measure the intercepted discharge and is collected in the same tank used for supplying water (recirculated). The model can simulate the roadway with the studied parameters, which are varied throughout this paper according to the following:

- Supplied discharge (Q): 10, 30, and 50 m^3/hr.
- Nozzle discharge (q): 5, and 12 m^3/hr.
- Longitudinal slope (S_L): 1.5%.
- Measurement Points: P1, P2, P3, and P4.

2.1. Experimental Error and Uncertainty

The accuracy of the experimental results depends on the precision and reliability of the instruments used and the consistency of the test procedure. All measurements were subject to instrumental and repeatability uncertainties, which were systematically analysed to assess their impact on the calculated hydraulic parameters such as velocity, depth, discharge, Reynolds number (Re), Froude number (Fr) (Rajaratnam, N., 1990; ISO/IEC., 2008).

Instrumental Uncertainties: The principal measuring devices employed in this study were the TSI - Laser Doppler Velocimeter (LDV) for point velocity, ultrasonic water level (UWL) sensors for flow depth, flowmeters for discharge regulation, and a V-notch weir for calibration. Each instrument's manufacturer-specified precision was adopted in the uncertainty analysis, following the recommendations of Subramanya, K. (2009) & Nalluri, C., & Featherstone, R. E. (2016), as shown in Table 1.

Table 1: Summarizes the instrumental uncertainties

Instrument	Measured variable	Precision	Uncertainty source
LDV (TSI)	Instantaneous velocity	±1.5%	Signal processing and optical alignment (Adrian,1991).
UWL sensor	Flow depth (h)	±0.3 mm	Electronic resolution and wave reflection
Flowmeter	Discharge (Q)	±2%	Calibration curve fitting
V-notch weir	Calibrated discharge	±1.5%	Head measurement error
Stopwatch	Time (t)	±0.1 s	Human reaction time

Repeatability uncertainties: For each flow condition, three repeated runs were conducted under identical boundary conditions to evaluate repeatability. The standard deviation (σ) and coefficient of variation (CV = σ/μ × 100%) were computed for velocity and depth (ISO/IEC., 2008). The mean CV values were less than 2.5% for velocity and 1.8% for depth, indicating good repeatability consistent with best laboratory particles reported by K. Subramanya (2009) & Rajaratnam (1990).

Combined uncertainty estimation: The total uncertainty (U_t) for a derived parameter (e.g., friction factor f or Reynolds number Re) was determined using the root-sum-square (RSS) method as shown in Eq. 1:

$$U_t = (U_Q^2 + U_h^2 + U_u^2)^{0.5} \quad (1)$$

Where:

U_Q- *uncertainty in discharge,*

U_h - *uncertainty in depth,*

U_u - *uncertainty in velocity*.

Applying this approach yielded typical combined uncertainties of: ±3.2% for mean velocity (U), ±3.8% for Re, and ±3.0% for Fr. These values fall within the acceptable limits for hydraulic flume experiments (Rajaratnam, 1990; Nalluri, C., & Featherstone, R. E., 2016).

Validation and confidence: Before experimentation, the entire measuring system was calibrated under steady uniform flow. The LDV measurements under uniform flow matched the logarithmic velocity law within ±2% deviation, confirming proper calibration and optical alignment. This comprehensive uncertainty assessment supports the reliability and reproducibility of the reported results.

3. Results and Discussion

3.1. Uniform Flow Results

To verify the accuracy of the experimental setup and instrumentation, velocity profiles were obtained along the channel centreline at a distance of 4 m from the upstream end. Measurements were conducted under three steady discharges of 10, 30, and 50 m^3/hr in the absence of spatially varied (SV) inflow. The experimental conditions associated with these baseline tests are summarized in Table 2.

Table 2: Experimental results without SV Inflow

Profile	Q (m^3/hr)	U (m/s)	h (m)	S_L	Fr	Re	u_*(m/s)
1	10	0.27	0.0067	0.015	1.05	7210	0.031
2	30	0.44	0.014	0.015	1.18	24329	0.045
3	50	0.67	0.028	0.015	1.31	71171	0.062

Baseline velocity distributions were first obtained in the absence of spatially varied (SV) inflow in order to provide a reference for identifying the influence of nozzle-induced inflow in subsequent experiments. Figure 6 presents the three velocity profiles measured at x = 4 m, expressed in wall coordinates U^+ and Y^+. All measurements were conducted with a Manning roughness coefficient of n = 0.016, representing a rough asphalt bed (Chow, V. T., 1959; Adrian, R. J., 1991; Subramanya, K., 2009). Figure 6 also includes the logarithmic velocity distribution equation, which characterizes the inertial sublayer region.

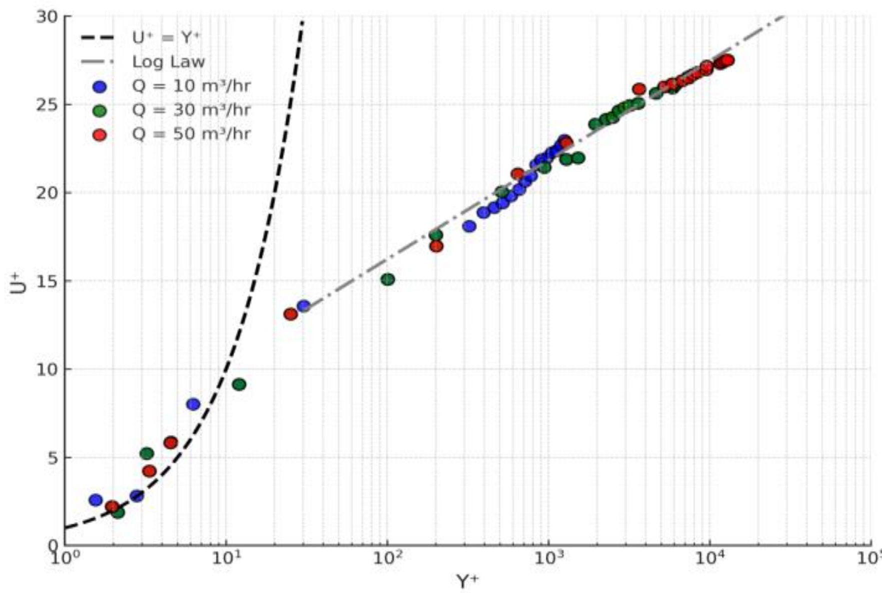

Figure 6: Comparison of experimental data with the universal velocity profile

The applicability of the logarithmic velocity distribution for uniform two-dimensional open-channel flows was confirmed by Miguntanna et al. (2020); Guo, J., & Julien, P. Y. (2013); Luchini, P. (2023). In this paper, the friction velocity (u*) was estimated using two independent approaches: from the velocity profile within the viscous sublayer ($Y^+ < 5$–10) and from a best-fit of the logarithmic law within the inertial sublayer ($30 < Y^+ < 0.2R^*$ or $y/h < 0.2$). The difference between the two estimates was within 2%, indicating a high level of consistency. The experimental data showed close agreement with the velocity distribution equation of, thereby confirming that both the physical model and the measuring instruments were properly calibrated and well suited for experiments involving spatially varied inflow (Kong et al., 2024; Wengrove & Foster, 2014; Quibeuf, 2020).

3.2. Spatially Varied Flow Results

The results of the spatially varied flow (SV) experiments are presented in multiple formats to highlight the different flow characteristics. To examine the applicability of the logarithmic law under the experimental configuration adopted in this paper, the velocity data were expressed in wall coordinates. The SV inflow experiments were performed with set of nozzles which installed normal to the model bed. The experimental conditions are summarized in Table 3. Base flows of 10, 30, and 50 m^3/hr were provided, representing the upstream discharge entering the model prior to the SV inflow zone.

Table 3: Summary of experimental conditions with SV inflow

Profile	Q (m^3/hr)	S_L	q (m^3/hr)	q_n (m^3/hr)	d_n (mm)	V_n (m/s)
1	10	0.015	5	0.41	20	0.37
2			12	1		0.89
3	30		5	0.41		0.37
4			12	1		0.89
5	50		5	0.41		0.37
6			12	1		0.89

Velocity profiles were obtained at eight distinct locations within the model. For defining the spatial coordinates of these measurement positions, the upper corner on the curb-opening side was designated as the origin (0,0), with the x-axis corresponding to the model length and the y-axis corresponding to the model width. Based on this reference system, the coordinates of the velocity profile measurement locations and nozzle locations are presented in Figure 7 and Table 4.

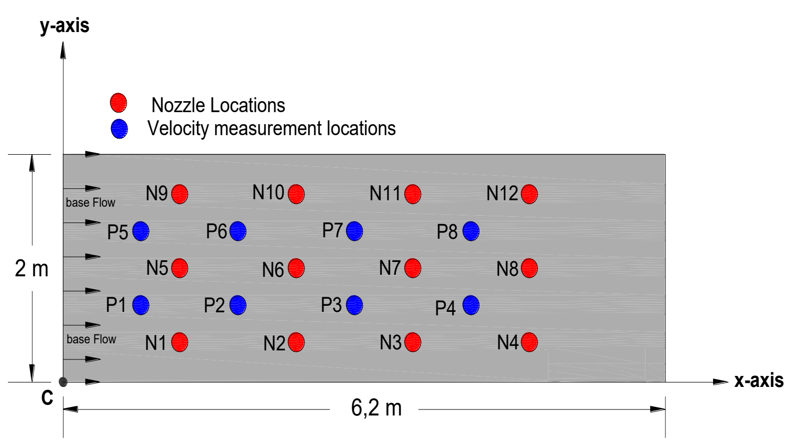

Figure 7: Schematic top view of the model indicating the velocity measurement positions & nozzle locations

Table 4: Coordinates of the velocity measurement locations and nozzle positions within the physical model

Point measurement information			Nozzles information		
Point name	x (m)	Point name	x (m)	Point name	x (m)
P1	0.8	0.675	N1	1.2	0.35
P2	1.8	0.675	N2	2.4	0.35
P3	3	0.675	N3	3.6	0.35
P4	4.2	0.675	N4	4.8	0.35
P5	0.8	1.325	N5	1.2	1
P6	1.8	1.325	N6	2.4	1
P7	3	1.325	N7	3.6	1
P8	4.2	1.325	N8	4.8	1
			N9	1.2	1.65
			N10	2.4	1.65
			N11	3.6	1.65
			N12	4.8	1.65

The nozzles that have the most impact on the measurement points will be explained in Table 5.

Table 5: Nozzles with predominant influence on the spatial distribution of measured velocities

Measurement Point Affected	Nozzle ID
P1	------
P2	N1, N5
P3	N1, N2, N5, N6
P4	N1, N2, N3, N5, N6, N7
P5	------
P6	N5, N9
P7	N5, N6, N9, N10

Figures 8 to 13 show the velocity profiles were measured at positions of P and the measurements were conducted at base flow (10, 30, and 50) m^3/hr and q = 5 and 12 m^3/hr.

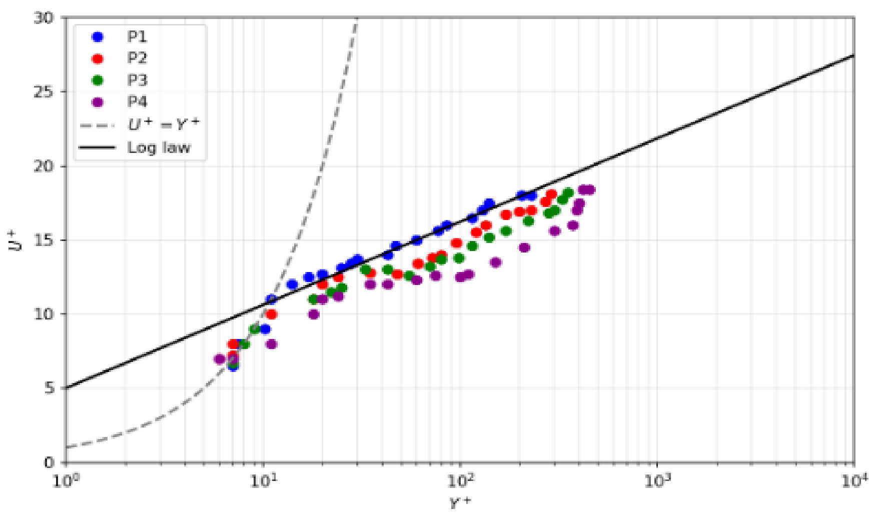

Figure 8: Velocity profiles in wall coordinates with SV inflow (q = 5m^3/hr), Q = 10 m^3/hr

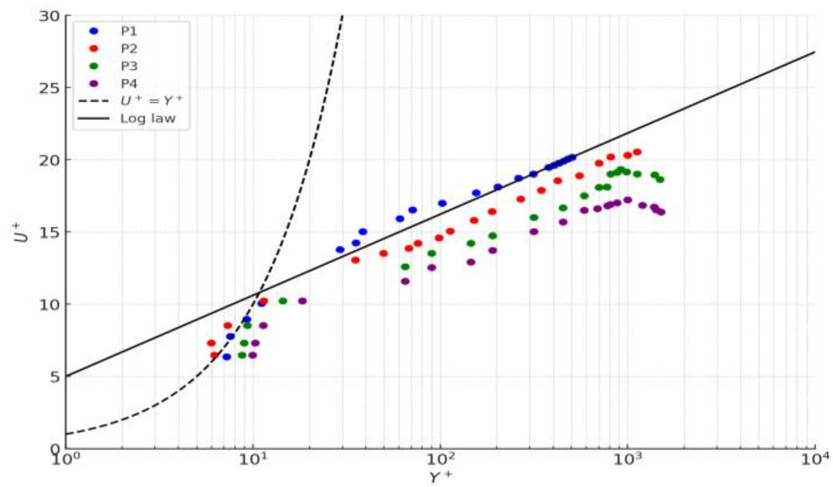

Figure 9: Velocity profiles in wall coordinates with SV inflow (q = 5m^3/hr), Q = 30 m^3/hr

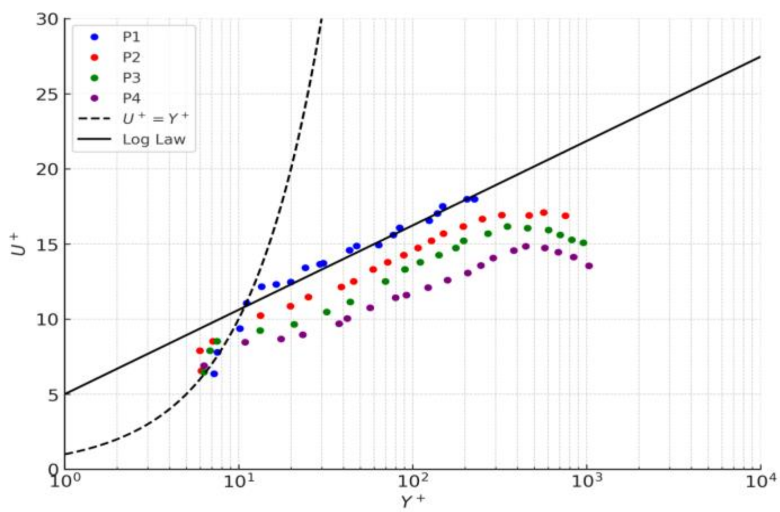

Figure 10: Velocity profiles in wall coordinates with SV inflow (q = 5m3/hr), Q = 50 m3/hr

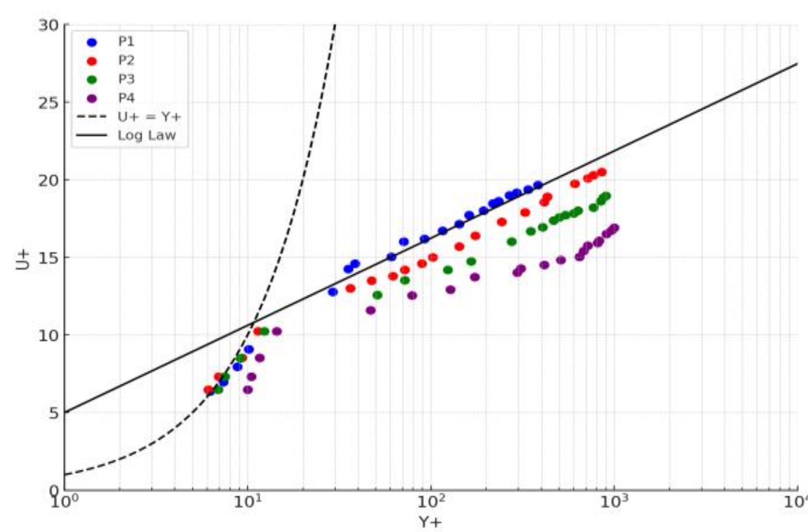

Figure 11: Velocity profiles in wall coordinate with SV inflow (q = 12 m3/hr), Q = 10 m3/hr

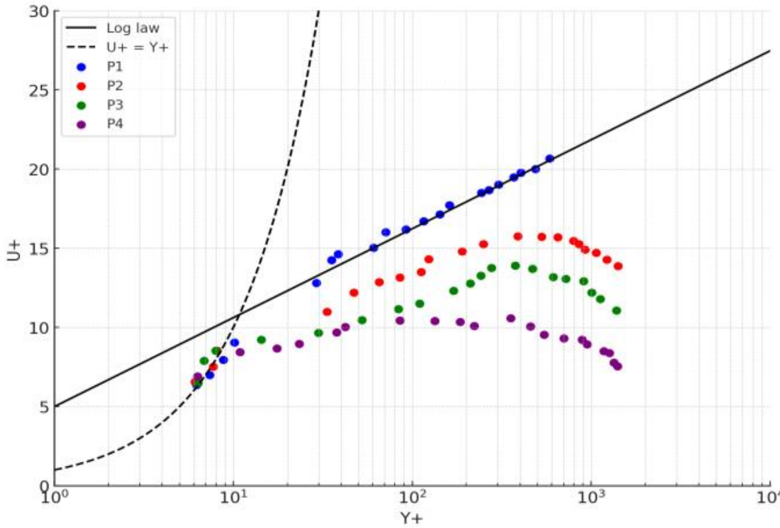

Figure 12: Velocity profiles in wall coordinate with SV inflow (q = 12 m^3/hr), Q = 30 m^3/hr

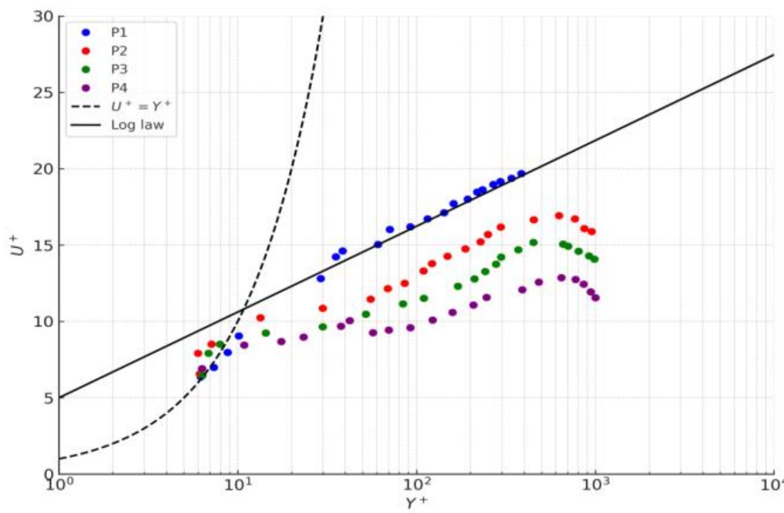

Figure 13: Velocity profiles in wall coordinate with SV inflow (q = 12m^3/hr), Q = 50 m^3/hr

Previous Figures show that the log law is valid within the inertial sublayer region close to the channel bed $Y^+ < 200$ for P1 because the locations of them before the nozzle impact zone, whereas the other data of P2, P3, and P4 fall below the line representing the log law. With the presence of SV inflow by increase in the nozzles affecting the flow, the degree that the data depart from the log law increases from the upstream toward the downstream of the model. The value of this deviation increases with the increase in the base discharge from 10 to 50 m^3/hr, and with the increase in the discharge of the nozzles from 5 to 12 m^3/hr toward the downstream of the model.

The deviations from the logarithmic velocity distribution observed under spatially varied inflow can be attributed to the hydrodynamic disturbance generated by the discrete nozzle inflows. Each nozzle introduces a small jet with higher momentum relative to the local near-bed flow, resulting in localized turbulence intensification and disruption of the equilibrium boundary-layer structure. The inflow increases Reynolds shear stress in the near-wall region and enhances vertical momentum exchange, which weakens the conditions required for the formation of a classical inertial sublayer. As additional nozzles contribute to inflow downstream, these disturbances accumulate, producing progressively larger departures from the log-law. This cumulative influence explains why deviations are small at P2, more pronounced at P3, and largest at P4.

The nozzle inflows increase local turbulence intensity and vertical mixing, producing stronger Reynolds shear stresses near the bed. These effects thicken the boundary layer and disturb the equilibrium conditions required for the log-law. As more nozzles contribute to inflow downstream, cumulative turbulence intensification increases, leading to progressively larger deviations from the universal velocity profile.

3.3. Velocity Profile Results

The measured velocities within the SV inflow zone are plotted in Figures 14 to 22, ignoring the measurements in P1 because it is before the area of SV inflow. These measurements were conducted over the full depth of flow. The velocity profiles have been normalized with V_n for q = 5 and 12 m^3/hr, V_n = 0.37 and 0.89 m/s, respectively.

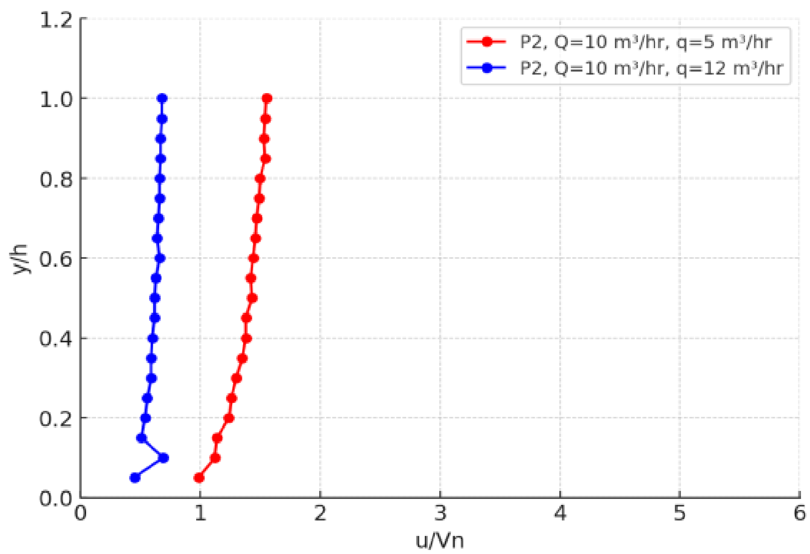

Figure 14: Normalized velocity profile (u/V_n vs. y/h) at P2 with Q = 10 m^3/hr and q = 5 and 12 m^3/hr

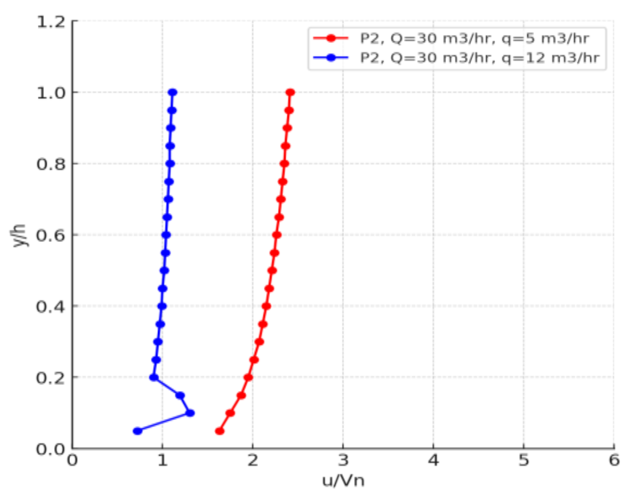

Figure 15: Normalized velocity profile (u/V_n vs. y/h) at P2 with Q = 30 m^3/hr and q = 5 and 12 m^3/hr

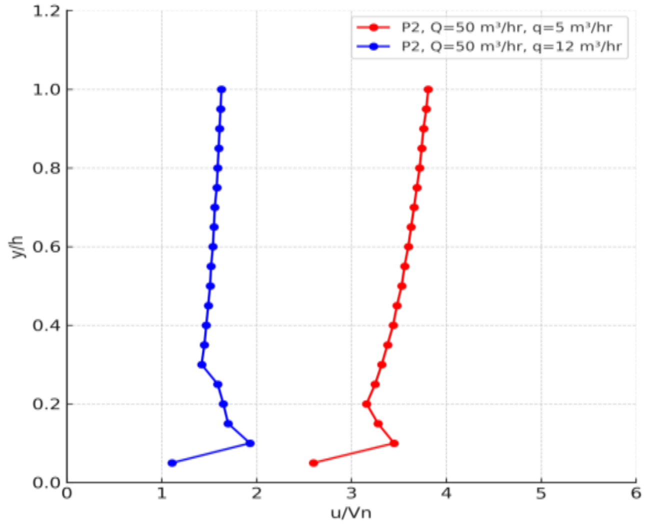

Figure 16: Normalized velocity profile (u/V_n vs. y/h) at P2 with Q = 50 m^3/hr and q = 5 and 12 m^3/hr

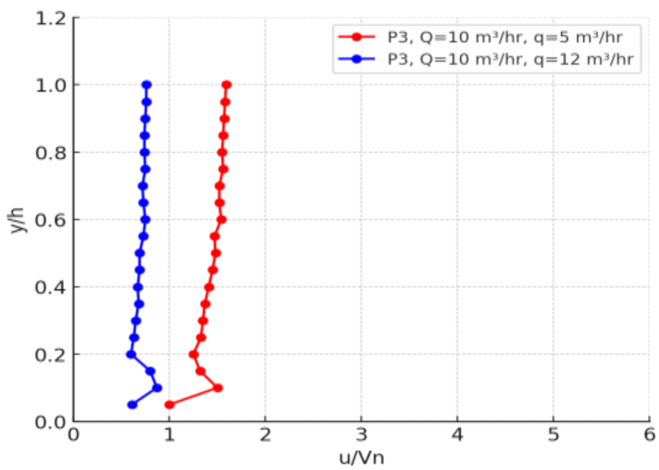

Figure 17: Normalized velocity profile (u/V_n vs. y/h) at P3 with Q = 10 m^3/hr and q = 5 and 12 m^3/hr

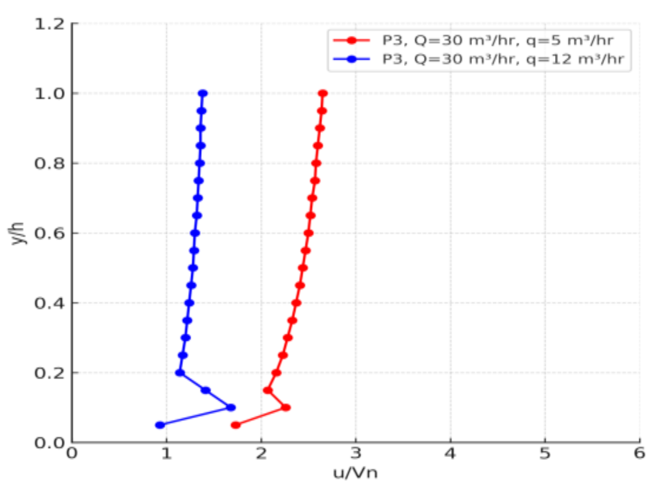

Figure 18: Normalized velocity profile (u/V_n vs. y/h) at P3 with Q = 30 m^3/hr and q = 5 and 12 m^3/hr

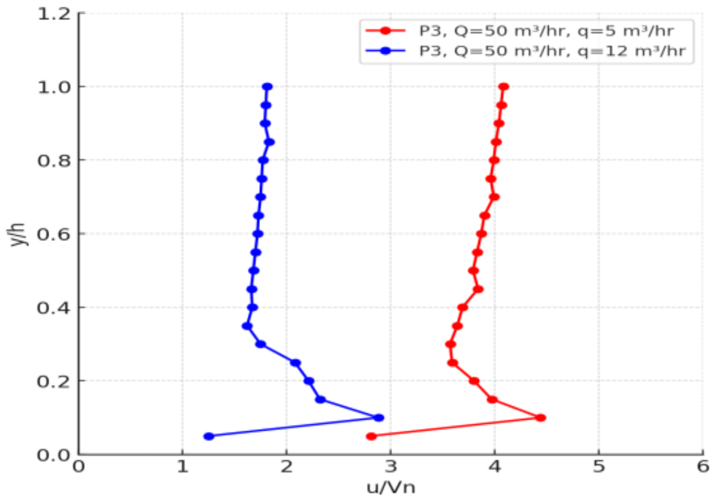

Figure 19: Normalized velocity profile (u/V_n vs. y/h) at P3 with Q = 50 m^3/hr and q = 5 and 12 m^3/hr

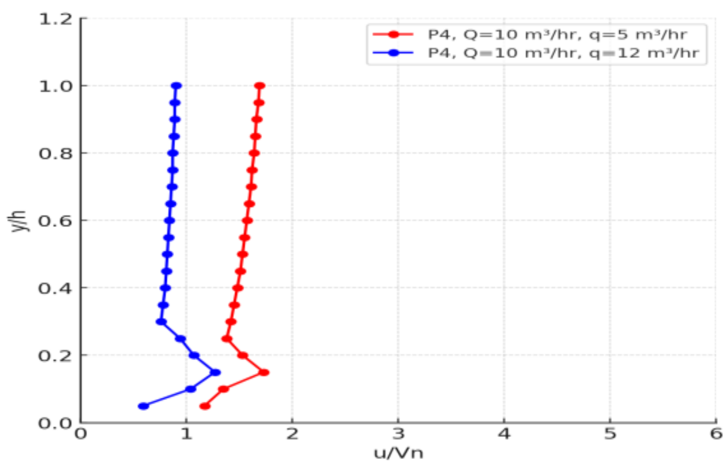

Figure 20: Normalized velocity profile (u/V_n vs. y/h) at P4 with Q = 10 m^3/hr and q = 5 and 12 m^3/hr

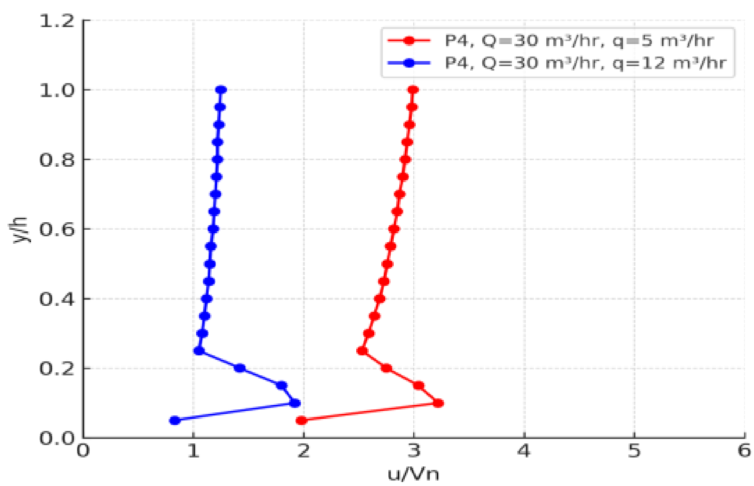

Figure 21: Normalized velocity profile (u/V_n vs. y/h) at P4 with Q = 30 m^3/hr and q = 5 and 12 m^3/hr

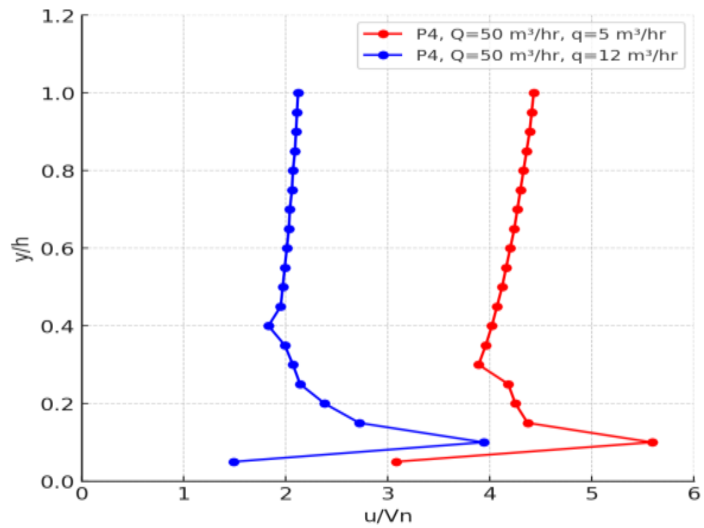

Figure 22: Normalized velocity profile (u/V_n vs. y/h) at P4 with Q = 50 m^3/hr and q = 5 and 12 m^3/hr

At location P1, the velocity distribution (u) is not significantly influenced by the spatial varied inflow, as this position lies upstream of the first nozzle. At P2, however, a slight effect is observed due to the inflow from two nozzles influencing this location. Further downstream, the nozzle-induced flow generates increasing disturbances, becoming more pronounced at P3 and reaching its maximum effect at P4.

As illustrated in the preceding Figures, the streamwise velocity (u) along the channel reaches its maximum value at approximately 0.1 of the total flow depth (h) at the measurement locations. This behavior results from the secondary flow (SV) inflow from nozzles, which generates a jet along the channel bed. Beyond this depth, the velocity gradient becomes negative, extending up to y/h = 0.2 or $Y^+ = 0.2R^*$. Above this region, a slight increase in velocity is observed.

The velocity profile downstream of each nozzle inflow shows the formation of wakes because when the fluid is discharged from a nozzle into the model, it interacts with the surrounding flow and creates zones of velocity deficit and turbulence zone. They often exhibit increased turbulence and mixing and remain localized near the inflow zone and gradually dissipate toward the downstream. These wakes do not propagate beyond the SV inflow zone. The effect of wake on the distribution of u reduces toward the downstream end of the SV inflow zone. This reflects the overall increase in velocity in the downstream direction. In simple terms, a wake can be thought of as the flow 'shadow' left behind the nozzle jet, which gradually smooths out as the flow continues downstream.

4. Dimensional Analysis

The velocity distribution in open-channel flow represents one of the most important aspects of hydraulic behavior, especially under spatially varied flow (SVF) conditions with increasing discharge. In such flows, the presence of lateral inflow significantly alters the local momentum balance, turbulence structure, and velocity gradients along both longitudinal and vertical directions. To characterize these complex interactions, dimensional analysis provides a systematic framework that relates the local velocity (u) to the governing geometric, hydraulic, and fluid properties. This approach is essential for identifying the governing parameters of both the prototype and its laboratory model. Once the geometric scale ratio between the model and prototype is defined, measurements collected from the experimental model can be translated to prototype conditions using appropriate dimensionless similarity criteria (Nalluri, C., & Featherstone, R. E., 2016). The local velocity u in SVF can be assumed to depend on the following independent variables, Eq. 2:

$$u = f\,(Q, q, S_C, S_L, h, x, b, y, g, \rho, \mu) \tag{2}$$

Where:
u - velocity of flow (LT^{-1}),
Q - base discharge ($L^3 T^{-1}$),
q - nozzle discharge ($L^3 T^{-1}$),
S_c - cross slope (dimensionless),
S_L - longitudinal slope (dimensionless),
h - flow depth (L),
x - distance along the flow direction (L),
b = channel width (L),
y = depth of flow where the velocity is measured (L),
g = gravity acceleration (LT^{-2}),
ρ = water density (ML^{-3}),
μ = dynamic viscosity of water ($ML^{-1} T^{-1}$).

By applying the Buckingham (π) theorem using (ρ), (V), and (h) as repeating variables, where (V) is mean velocity), we obtain the following dimensionless groups, Eq. 3:

$$u = \alpha\, (y/h)^a\, (x/h)^b\, (q/Q)^c\, (h/b)^d\, (SL)^e\, (Fr)^i\, (Re)^k \tag{3}$$

The empirical relationship for velocity of flow (u) was developed using SPSS and Multiple Nonlinear Regression (MNLR), a widely adopted approach in hydraulic modeling to quantify the influence of flow and geometric parameters (Nezu, I., & Rodi, W. 1986; Tiğrek, Ş., & Sipahi, S. 2012; Alfatlawi, 2021). The coefficients (α, a, b, c, d, e, i, k) were determined experimentally based on laboratory data following the principles of turbulent flow similarity. Table 6 displays the statistical importance of each parameter category.

Table 6: Regression coefficient values

Parameter	Symbol	Coefficient	Effect	Significance
----	α	1.17	Scaling factor	Represent baseline velocity
y/h	a	0.097	Slight increase	Weak
x/h	b	0.019	Negligible	Weak
q/Q	c	0.034	Marginal	Weak
h/b	d	0.63	Strong increase	Significant
S_L	e	-0.65	Moderate decrease	Significant
Fr	i	0.82	Strong increase	Highly Significant

The regression exponents in Table 6 can be interpreted in terms of the underlying hydraulic behavior. The scaling coefficient (α ≈ 1.17) provides a baseline consistent with the order of magnitude of the measured velocities. The small positive exponent for the relative depth (y/h) (a ≈ 0.097) indicates a mild increase of velocity with distance from the bed within the inner portion of the flow, in line with boundary-layer theory. The very small exponent associated with the longitudinal coordinate (x/h) (b ≈ 0.019) suggests that, over the length of the SVF zone, the direct influence of x is weak once discharge, depth and Froude number are considered. The exponent for the inflow ratio (q/Q) (c ≈ 0.034) is positive but modest, reflecting the slight enhancement of local velocity due to the added momentum of the nozzle inflows.

The stronger dependence on the aspect ratio (h/b) (d ≈ 0.63) shows that velocity is more sensitive to relative flow depth, as thicker flow layers weaken the relative influence of the boundaries and favour higher core velocities. The negative exponent for longitudinal slope (S_L) (e ≈ –0.65) indicates that, within the tested slope range, increased bed slope is associated with a redistribution of shear and enhanced near-bed dissipation, which tends to reduce local velocity at the measurement section when other variables are held constant. Finally, the relatively large positive exponent for the Froude number (Fr) (i ≈ 0.82) confirms the strong role of inertial effects, with higher Fr producing higher local velocities. The influence of Reynolds number was found to be statistically small within the fully turbulent regime investigated and was therefore not retained explicitly in the final expression.

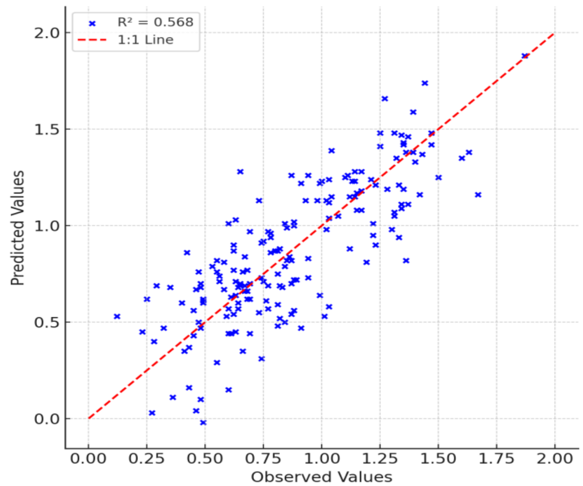

Figure 23: Observed verses predicted values of velocity

Table 7: Quantitative statistical coefficients to investigate model accuracy

Coefficient	Obtained value	Optimal value
R^2	0.5620	1, -1
d	0.7620	1
MAE	0.3070	0
NSE	0.06	1

Table 7 summarizes the statistical indicators used to assess the predictive performance of the developed model for point velocity. The obtained coefficient of determination (R^2 = 0.5620) indicates that approximately 56 % of the variability in the measured velocities is explained by the model, reflecting a moderate correlation between observed and predicted values (Dakheel et al., 2024). Such a level of agreement is reasonable, considering that flow behavior in open channels is inherently complex, nonlinear, and influenced by several uncontrolled factors such as turbulence, secondary currents, and local flow disturbances. The index of agreement (d = 0.7620) further confirms a reasonable correspondence, suggesting that the model reproduces the general trend of the experimental data with acceptable accuracy (Willmott, C. J., 1981; Willmott et al., 1985). The mean absolute error (MAE = 0.3070) demonstrates that the average deviation between observed and predicted velocities is relatively small, though not negligible. However, the Nash–Sutcliffe efficiency (NSE = 0.06) reflects that the predictive skill of the model is only marginally better than using the mean of the observations, revealing limited efficiency in reproducing the detailed variation of point velocities (Nash, J. E., & Sutcliffe, J. V., 1970). Overall, these results indicate that the model provides a fair estimation of velocity behavior within the spatially varied flow but requires further refinement such as enhanced calibration or inclusion of additional hydraulic parameters—to improve its predictive reliability.

5. Conclusion

This paper presents an experimental investigation into the hydraulic behavior of roadway flow, with particular emphasis on conditions near curb-opening inlets. A physical model on a 1:1 scale was used to conduct a number of experimental investigations on a range of discharges and longitudinal slopes.

The results of the velocity profiles indicate that the logarithmic law is valid within the inertial sublayer near the channel bed (Y+ < 200) at locations P1 and P5, as these lie upstream of the nozzle impact zone. In contrast, the velocity distributions at P2, P3, and P4 fall below the line representing the log law. The presence of spatially varied inflow enhances the degree of deviation from the log law, with the discrepancy increasing progressively from the upstream to the downstream regions of the channel. Furthermore, the magnitude of deviation intensifies both with an increase in the base discharge (from 10 to 50 m^3/hr) and with higher nozzle discharge (from 5 to 12 m^3/hr).

At location P1, the velocity of flow (u) remains largely unaffected by the spatially varied flow, as this point is situated upstream of the first nozzle. A slight influence is observed at P2, where the inflow from two nozzles begins to change the velocity distribution. Progressing downstream, the disturbances generated by the nozzle-induced flow intensify, becoming more obvious at P3 and reaching their maximum effect at P4.

The analysis demonstrates that the flow velocity (u) attains its maximum at approximately 0.1 of the total flow depth (h) across the measurement locations, primarily due to the secondary flow (SV) inflow from the nozzles, which produces a jet along the channel bed. Beyond this depth, the velocity gradient decreases. Above this region, only a slight recovery in velocity is observed, confirming the localized influence of nozzle-induced inflow on the velocity profile.

The velocity profiles downstream of the nozzle inflows reveal the development of wakes, formed as the discharged jets interact with the base flow and generate localized regions of velocity deficit and increased turbulence. These wakes are characterized by enhanced mixing and remain confined to the nearness of the inflow zone, gradually dissipating with distance downstream. Their influence does not extend beyond the spatially varied inflow region, and the effect on the distribution of streamwise velocity (u) diminishes toward the downstream end of this zone. This behavior corresponds to the overall increase in velocity observed in the longitudinal direction. In essence, the wake may be regarded as a temporary 'shadow' of reduced velocity behind each jet, which progressively smooth out as the flow continues downstream.

Acknowledgments

We would like to thank the University of Babylon, College of Engineering, for providing all the necessary facilities to complete this paper.

Author Contributions

All authors contributed equally to the preparation of this article.

Disclosure of Interest

The authors declare that they have no known competing financial interests or personal relationships that could have appeared to influence the work reported in this paper.

Data Availability Statement

The data that support the findings of this study are available from the corresponding author upon reasonable request.

Funding Source

This study didn’t receive any specific funds.

References

Kemper, S., & Schlenkhoff, A. (2019). Experimental study on the hydraulic capacity of grate inlets with supercritical surface flow conditions. Water Science and Technology, 79(9), 1717–1726. https://doi.org/10.2166/wst.2019.171.

Gómez, M., & Russo, B. (2009). Hydraulic efficiency of continuous transverse grates for paved areas. Journal of Irrigation and Drainage Engineering, 135(2), 225–230. https://doi.org/10.1061/(ASCE)0733-9437(2009)135:2(225).

Pedro, L., Jorge L., Rita, F. C., Russo, B., & Gómez, M. (2016). Assessment of the ability of a volume of fluid model to reproduce the efficiency of a continuous transverse gully with grate. Journal of Irrigation and Drainage Engineering, 142(9), 04016039. https://doi.org/10.1061/(ASCE)IR.1943-4774.0001058.

Alfatlawi, T. J., Naji, A., Hamid, Z., & Hussein, M. (2021). Grate inlet hydraulic efficiency with varying porous asphalt aprons. Journal of Irrigation and Drainage Engineering, 147(10), 04021034. https://doi.org/10.1061/(ASCE)IR.1943-4774.0001554.

Russo, B. (2010). Design of surface drainage systems according to hazard criteria related to flooding in urban areas. Thesis (PhD). School of Civil Engineering, UPC, Barcelona, Spain.

Garcia, A., Aboufoul, M., Asamoah, F., & Jing, D. (2019). Study the influence of the air void topology on porous asphalt clogging. Construction and Building Materials, 227, 116791. https://doi.org/10.1016/j.conbuildmat.2019.116791.

Tiğrek, Ş., & Sipahi, S. (2012). Rehabilitation of storm water collection systems of urban environment using the small roads as conveyance channels. International Journal of Environmental Science and Technology, 9(1), 95–103. DOI: 10.1007/s13762-011-0002-x.

Russo, B., Gómez, M., & Tellez, J. (2013). Methodology to estimate the hydraulic efficiency of nontested continuous transverse grates. Journal of Irrigation and Drainage Engineering, 139(10), 864–871. https://doi.org/10.1061/(ASCE)IR.1943-4774.0000625.

Comport, B. C., & Thornton, C. I. (2012). Hydraulic efficiency of grate and curb inlets for urban storm drainage. Journal of Hydraulic Engineering, 138(10), 878–884. https://doi.org/10.1061/(ASCE)HY.1943-7900.0000552.

Khiadani, M. H., Kandasamy, J. & Beecham, S. (2007). Velocity distributions in spatially varied flow with increasing discharge. Journal of Hydraulic Engineering, 133(7), 721–728. https://doi.org/10.1061/(ASCE)0733-9429(2007)133:7(721).

Beecham, S., Khiadani, M. H., & Kandasamy, J. (2005). Friction factors for spatially varied flow with increasing discharge. Journal of Hydraulic Engineering, 131(9), 792–799. https://doi.org/10.1061/(ASCE)0733-9429(2005)131:9(792).

Nezu, I., & Rodi, W. (1986). Open-channel flow measurements with a laser Doppler anemometer. Journal of Hydraulic Engineering, 1125, 335–355. https://doi.org/10.1061/(ASCE)0733-9429(1986)112:5(335).

Nezu, I., & Nakagawa, H. (1993). Turbulence in open-channel flows. IAHR Monograph Series, Balkema, Rotterdam, The Netherlands.

Van Driest, E. R. (1956). On turbulent flow near a wall. Journal of the Aeronautical Sciences, 23(11), 1007–1011.

Henderson, F. M. (1966). Open channel flow. Macmillan.

Chow, V. T. (1959). Open-channel hydraulics. McGraw-Hill.

Subramanya, K. (2009). Flow in open channels (3rd ed.). Tata McGraw-Hill.

Adrian, R. J. (1991). Particle-imaging techniques for experimental fluid mechanics. Annual Review of Fluid Mechanics, 23(1), 261–304. https://doi.org/10.1146/annurev.fl.23.010191.001401.

Bonnett J. P., Gresillon, D., Cabrit, B. & Frolov, V. (1995). Collective light scattering as non-particle laser velocimetry. Meas. Sci. Technol. 6 620. DOI: https://doi.org/10.1088/0957-0233/6/6/002.

Tajikawa, T., Kohri, S., Mouri, T., Fujimi, T., Yamaguchi, H., & Ohba, K. (2024). Development of miniaturised fibre-optic laser doppler velocimetry for opaque lubrication system. Photonics, 11(9), 892. https://doi.org/10.3390/photonics11090892.

Mohammed Alabas (2025). Experimental Study of the Coefficient of Discharge for Porous Stepped Spillways. Civil and Environmental Engineering, 21(1), 570–580. https://doi.org/10.2478/cee-2025-0043.

Rajaratnam, N. (1990). Hydraulics laboratory manual. University of Alberta Press.

ISO/IEC. (2008). Guide to the expression of uncertainty in measurement (GUM). International Organization for Standardization.

Nalluri, C., & Featherstone, R. E. (2016). Civil engineering hydraulics (6th ed.). John Wiley & Sons.

Garrote, J., et al. (2021). The Manning's roughness coefficient calibration method for hydrodynamic models. Applied Sciences, 11(19), 2967. https://doi.org/10.3390/app11199267.

Miguntanna, N., Moses, H., Sivakumar, M., Yang, S. Q., Enever, K., & Riaz, M. Z. B. (2020). Re-examining log law velocity profile in smooth open channel flows. Environmental Fluid Mechanics, 20(2), 367–385. https://doi.org/10.1007/s10652-019-09733-6.

Guo, J., & Julien, P. Y. (2013). Modified log-wake law for smooth rectangular open channel flow. Journal of Hydraulic Research, 52(1), 121–128. https://doi.org/10.1080/00221686.2013.818584.

Luchini, P. (2023). Uniform representation of the turbulent velocity profile in an open channel. arXiv preprint. https://arxiv.org/abs/2310.11542.

Kong, J., Nugroho B., Bennetts, L. G., Chan, C. I. & Chin, R. C. (2024). Friction velocity determination techniques in turbulent boundary layers with miniature vortex generators. Experiments in Fluids, 65 (76). https://doi.org/10.1007/s00348-024-03817-w.

Wengrove, M. E. & Foster, D. L. (2014). Field evidence of the viscous sublayer in a tidally forced developing boundary layer. Geophysical Research Letters, 41, 5084–5090. https://doi.org/10.1002/2014GL060709.

Quibeuf, G., Charru, F., & Lacaze, L. (2020). Particle motion within the viscous sublayer of a turbulent shear flow. Physical Review Fluids, 5, 014306. https://doi.org/10.1103/PhysRevFluids.5.014306.

Dakheel, A., Ismaeel, A., & Makki, J. (2024). Numerical modelling of local scour depth at non-uniform piers. Civil and Environmental Engineering, 20.2, pp. 699-710. https://doi.org/10.2478/cee-2024-0052.

Willmott, C. J. (1981). On the validation of models. Physical Geography, 2(2), 184–194. https://doi.org/10.1080/02723646.1981.10642213.

Willmott, C. J., Ackleson, S. G., Davis, R. E., Feddema, J. J., Klink, K. M., Legates, D. R., O’Donnell, J., & Rowe, C. M. (1985). Statistics for the evaluation and comparison of models. Journal of Geophysical Research: Oceans, 90(C5), 8995–9005. https://doi.org/10.1029/JC090iC05p08995.

Nash, J. E., & Sutcliffe, J. V. (1970). River flow forecasting through conceptual models: Part I—A discussion of principles. Journal of Hydrology, 10(3), 282–290. https://doi.org/10.1016/0022-1694(70)90255-6.

How to Cite This Article

Hasan, Z. H., & A Alabas, M. A. A. (2026). Flow Velocity Distribution near Curb-opening Inlets: Experiments and Analysis. Civil and Environmental Engineering, 0 (0). https://doi.org/10.2478/cee-2026-0069